Maneuvering Target Detection Based on Three-Dimensional Coherent Integration

LANGXU ZHAO[ID], HAIHONG TAO[ID], AND WEIJIA CHEN
National Laboratory of Radar Signal Processing, Xidian University, Xi'an 710071, China

Corresponding author: Haihong Tao (hhtao@xidian.edu.cn)

ABSTRACT Due to the target motion, range cell migration (RCM) and Doppler frequency migration (DFM) always occur. That is harmful to the signal enhancement and detection. In order to solve the problem, a novel three-dimensional (3-D) coherent integration (TDCI) based algorithm is proposed in this article which consists of three stages. Firstly, a 3-D space is generated by the autocorrelation function. After that, TDCI algorithm is realized and TDCI domain is obtained in which the motion parameters can be accurately estimated. Finally, compensating off the RCM and DFM by the estimates, the target signal can be accumulated and detected in range-Doppler frequency domain. Theoretical analyses and simulation experiments are given to demonstrate that the proposed algorithm is able to deal with the problems of velocity ambiguity, shadow effect, and cross-term with superior resolution. Comparisons with several representative algorithms lead us to the conclusion that the proposed algorithm can strike a good balance between computation cost and anti-noise performance. In the end, real measured data processing and result analysis are carried out, which further verify the effectiveness of the proposed algorithm.

INDEX TERMS Coherent integration, Doppler frequency migration, parameter estimation, range cell migration, maneuvering target detection.

I. INTRODUCTION

With the development of radar filed, maneuvering target detection and parameter estimation have received a growing attention [1]–[5]. High speed, low signal to noise ratio (SNR), and multiple targets are three main problems against the radar performance. High speed may lead to range walk and velocity ambiguity, degrading the detection performance and parameter estimation accuracy. Low SNR causes poor target detection probability directly. In the multi-target scenario, some weak targets may be missed due to the shadow effect. Besides, false alarms may occur in the nonlinear algorithms affected by cross-terms. Long-time integration can effectively improve the radar performance which can be generally categorized into two kinds: incoherent integration and coherent integration [6], [7]. Incoherent integration based algorithms such as Hough transform [8]–[10], Radon transform [11] and track-before-detection [12] are relatively easy to implement

with low computation costs, since they employ only amplitude information without strict phase adjustments. In general, their performance is less efficient as compared to the coherent integration based algorithms. Coherent integration based algorithms utilize both amplitude and phase information with relatively high computation complexities. Thus, their performance is more advantageous. Notably, Long time integration based algorithms always encounter two main problems: range cell migration (RCM) and Doppler frequency migration (DFM) [13], [14], deteriorating their focusing performance. Thus, for better integration gain, RCM and DFM issues need to be resolved.

As to the target with uniform motion, three representative algorithms are mentioned including keystone transform (KT) [15], [16], axis rotation-moving target detection (AR-MTD) [17], [18], and Radon-Fourier transform (RFT) [19]–[21]. KT can blindly correct RCM and effectively achieve coherent integration. However, its performance may suffer from degradation in the case of Doppler ambiguity. AR-MTD and RFT are implemented by two-dimensional

searching process. Accordingly, their computation costs may be high. Moreover, these three algorithms will perform poorly while dealing with the target with high-order motion because of their invalidity for DFM.

Recently, many algorithms have been developed for the target with acceleration motion. KT-fractional FT (KT-FRFT) [22] and improved AR-FRFT (IAR-FRFT) [23] are two popular algorithms. They coherently integrate the target signal by eliminating RCM and DFM separately. Since KT and IAR are unable to tackle the RCM caused by the acceleration completely, part of the integration gain may be lost. In order to completely remove RCM and DFM simultaneously, several three-dimensional (3-D) searching based algorithms are proposed, such as maximum likelihood (ML) based algorithm [24] and Radon based algorithms (including Radon-FRFT (RFRFT) [25], Radon-Lv's distribution (RLVD) [26], and generalized RFT (GRFT) [27], [28]). ML based algorithm builds ML function and determines targets by its poles in the parameter space. Radon based algorithms are implemented by accumulating the targets signals along their trajectories. Nevertheless, the high computation burden and severe false alarm induced by the 3-D ergodic searching process and blind speed sidelobe limit their application. In order to avoid searching, symmetric autocorrelation function-scaled FT (SAF-SFT) [29], 3-D scaled transform (TDST) [30], scaled nonuniform fast FT-scaled periodic discrete FT (SNUFFT-SPDFT) [31], product scaled periodic LVD (PSP-LVD) [32] and the algorithm proposed in [33] are studied. These algorithms can effectively deal with the maneuvering targets. Unfortunately, they may be inappropriate for the low-SNR scenario. Besides, some algorithms are proposed for the array radar system [34].

In this article, a novel 3-D coherent integration (TDCI) based detection algorithm is proposed. The proposed algorithm accurately estimates the motion parameters in TDCI domain, which helps to completely eliminate the RCM and DFM. Thereafter, the target signal is coherently integrated and detected via constant false alarm rate (CFAR) technology in range-Doppler frequency domain. Both the theories and simulations illustrate its superior resolution and cross-term suppression capability. Compared with several existing algorithms on computation complexity, detection capability, and parameter estimation accuracy, the proposed algorithm can effectively ease the computation burden with acceptable anti-noise performance. Finally, a set of real measured data is processed to further demonstrate the effectiveness of the proposed algorithm.

The rest of this article is organized as follow: Section II establishes the mathematical model for the received target signal. Section III introduces the theory and main procedure of the proposed algorithm. In Section IV, we give some analyses for the proposed algorithm, including integration capability, cross-term suppression, theoretical resolution, efficient implementation, and computation complexity. In Section V, simulated and real data are processed and some performance

comparisons are carried out. Finally, conclusions are given in Section VI.

II. SIGNAL MODEL

Suppose the radar transmits a linear frequency modulated signal with the form

$$p(t) = rect\left(\frac{t}{T_p}\right) \exp\left[j2\pi\left(f_c t + \frac{1}{2}\gamma t^2\right)\right] \quad (1)$$

where $rect(u)$ represents the rectangular pulse function expressed as

$$rect(u) = \begin{cases} 1, & |u| \le 0.5 \\ 0, & |u| > 0.5. \end{cases} \quad (2)$$

where t denotes the fast time variable, T_P denotes the pulse width, f_c denotes the carrier frequency, γ denotes the chirp rate.

Assuming that K targets appear in the radar surveillance area, the received signal after down conversion can be represented as

$$s_r(t, t_m) = \sum_{k=1}^{K} A_{1k} rect\left(\frac{t - \tau_k}{T_p}\right) \exp\left(-j2\pi f_c \tau_k\right)$$
$$\times \exp\left[j\pi\gamma(t - \tau_k)^2\right] \quad (3)$$

where t_m denotes the azimuth slow time variable, $A_{1\,k}$ denotes the amplitude of the k-th target signal, $\tau_k = 2R_k(t_m)/c$ denotes the time delay, c denotes the speed of light, $R_k(t_m)$ denotes the instantaneous radial range between the k-th target and the radar which can be expressed as

$$R_k(t_m) = R_{0k} + v_k t_m + \frac{1}{2}a_k t_m^2 \quad (4)$$

where R_{0k} denotes the initial radial range between the k-th target and the radar, v_k and a_k denote the radial velocity and acceleration, respectively. After pulse compression (PC), the signal can be formulated as

$$s_{pc}(t, t_m) = \sum_{k=1}^{K} A_{2k} \sin c\left[B\left(t - \frac{2R_{0k} + 2v_k t_m + a_k t_m^2}{c}\right)\right]$$
$$\times \exp\left(-j2\pi f_c \frac{2R_{0k} + 2v_k t_m + a_k t_m^2}{c}\right) \quad (5)$$

where $A_{2\,k}$ denotes the amplitude, $\sin c(\cdot)$ denotes the sinc function, B denotes the bandwidth.

Then, the Doppler frequency of the k-th target signal can be obtained, expressed as

$$f_d = -\frac{2v_k + 2a_k t_m}{\lambda} \quad (6)$$

where $\lambda = c/f_c$ denotes the wavelength. From (5) and (6), it is clearly that the envelopes of the target signals walk across the range units and the Doppler frequencies are linear time varying, i.e. both RCM and DFM occur, which will seriously affect the radar detection and parameter estimation.

III. NOVEL TDCI BASED DETECTION ALGORITHM

As mentioned above, RCM and DFM seriously affect the radar performance. Fortunately, according to the signal model, they can be completely compensated by accurate parameter estimates. Thereafter, the target signal can be integrated and detected in range-Doppler frequency domain. Motivated by this idea, a novel TDCI based detection algorithm is proposed in this section.

A. TDCI ALGORITHM FOR PARAMETER ESTIMATION

By performing FT to (5) along t-axis, the signal is transformed into range frequency domain.

$$s_f(f, t_m) = \sum_{k=1}^{K} A_{3k} \, rect\left(\frac{f}{B}\right)$$

$$\times \exp\left[-j2\pi(f+f_c)\frac{2R_{0k}+2v_k t_m+a_k t_m^2}{c}\right] \quad (7)$$

where f denotes the range frequency variable, A_{3k} denotes the amplitude.

In (7), $2v_k t_m$ and $a_k t_m^2$ are coupled with $f+f_c$, leading to the RCM and DFM, which makes it impossible to achieve coherent integration and parameter estimation directly. Define an autocorrelation function (AF) as

$$R(f, t_m, \tau_m) = s_f\left[f, t_m+\left(\tau_m+\frac{h}{2}\right)\right]$$

$$\cdot s_f\left[f, t_m-\left(\tau_m+\frac{h}{2}\right)\right] \quad (8)$$

where τ_m denotes the lag time variable, h denotes a constant delay. Similar to the analysis in [35], in order to achieve the best anti-noise capability, h should be set above the integration time T. Substituting (7) into (8), one has

$$R(f, t_m, \tau_m)$$

$$= \sum_{k=1}^{K} A_{3k}^2 \, rect\left(\frac{f}{B}\right)$$

$$\times \exp\left\{-j2\pi\left(\frac{f+f_c}{f_c}\right)\frac{4R_{0k}+4v_k t_m+2a_k\left[t_m^2+\left(\tau_m+\frac{h}{2}\right)^2\right]}{\lambda}\right\}$$

$$\underbrace{\qquad\qquad\qquad\qquad\qquad\qquad\qquad}_{auto-terms}$$

$$+ \sum_{i=1}^{K}\sum_{j=i+1}^{K} R_{cross,i,j}(f, t_m, \tau_m) \quad (9)$$

where $R_{cross,i,j}(f, t_m, \tau_m)$ denotes the cross-term generated by the i-th and j-th targets, expressed as

$$R_{cross,i,j}(f, t_m, \tau_m)$$

$$= 2A_{3i}A_{3j} \, rect\left(\frac{f}{B}\right)$$

$$\times \exp\left\{-j2\pi\left(\frac{f+f_c}{f_c}\right)\frac{4\Delta R_0+4\Delta v t_m+2\Delta a\left[t_m^2+\left(\tau_m+\frac{h}{2}\right)^2\right]}{\lambda}\right.$$

$$\times \cos\left\{2\pi\left(\frac{f+f_c}{f_c}\right)\frac{4\nabla v\left(\tau_m+\frac{h}{2}\right)+4\nabla a t_m\left(\tau_m+\frac{h}{2}\right)}{\lambda}\right\} \quad (10)$$

where $\Delta R_0=(R_{0i}+R_{0j})/2$, $\Delta v=(v_i+v_j)/2$, $\Delta a=(a_i+a_j)/2$, $\nabla v=(v_i-v_j)/2$, $\nabla a=(a_i-a_j)/2$.

Then, the 1st coherent integration along the τ_m-axis is achieved via the following scaled transform.

$$C_1(f, t_m, f_{\tau m})$$

$$= \int R(f, t_m, \tau_m) \exp\left[j2\pi\left(\frac{f+f_c}{f_c}\right)f_{\tau m}\left(\tau_m+\frac{h}{2}\right)^2\right]d\tau_m$$

$$= \sum_{k=1}^{K} A_{4k} \, rect\left(\frac{f}{B}\right)$$

$$\times \exp\left[-j2\pi\left(\frac{f+f_c}{f_c}\right)\frac{4R_{0k}+4v_k t_m+2a_k t_m^2}{\lambda}\right]\delta\left(f_{\tau m}-\frac{2a_k}{\lambda}\right)$$

$$+ \sum_{i=1}^{K}\sum_{j=i+1}^{K} C_{1-cross,i,j}(f, t_m, f_{\tau m}) \quad (11)$$

where $f_{\tau m}$ denotes the scaled frequency variable with respect to τ_m, A_{4k} denotes the amplitude, $\delta(\cdot)$ denotes the Dirac delta function, $C_{1-cross,i,j}(f, t_m, f_{\tau m})$ denotes the cross-term.

Afterwards, the coupling between f and t_m^2 can be removed by multiplying an exponential term to (11), presented as

$$C_1^*(f, t_m, f_{\tau m})$$

$$= C_1(f, t_m, f_{\tau m}) \times \exp\left[j2\pi\left(\frac{f+f_c}{f_c}\right)f_{\tau m}t_m^2\right] \quad (12)$$

From (11), we acquire an important point: due to the integration, the energies of the auto-terms are concentrated into planes $f_{\tau m}=2a_k/\lambda(k=1,2\ldots K)$. Thus, the multiplication in (12) can be considered approximately equivalent to

$$C_1^*(f, t_m, f_{\tau m})$$

$$= \sum_{k=1}^{K} A_{4k} \, rect\left(\frac{f}{B}\right)$$

$$\times \exp\left[-j2\pi\left(\frac{f+f_c}{f_c}\right)\frac{4R_{0k}+4v_k t_m}{\lambda}\right]\delta\left(f_{\tau m}-\frac{2a_k}{\lambda}\right)$$

$$+ \sum_{i=1}^{K}\sum_{j=i+1}^{K} C_{1-cross,i,j}^*(f, t_m, f_{\tau m}) \quad (13)$$

where $C_{1-cross,i,j}^*(f, t_m, f_{\tau m})$ denotes the cross-term. It can be observed that the coupling is removed.

When $|4v_k/\lambda| > PRF/2$, autocorrelation velocity ambiguity occurs, and v_k should be rewritten as

$$v_k = N_k v_{ab} + v_{0k} \quad (14)$$

where N_k denotes the autocorrelation fold factor, $v_{ab} = PRF \times \lambda/4$ denotes the autocorrelation blind velocity, $|v_{0k}| < v_{ab}/2$ denotes the autocorrelation base band velocity.

Considering the special equation $\exp\left(-j2\pi 4N_k v_{ab} t_m / \lambda\right) = 1$, (13) must be rewritten as

$$
\begin{aligned}
&C_1^*\left(f, t_m, f_{\tau m}\right) \\
&= \sum_{k=1}^{K} A_{4k} \, rect\left(\frac{f}{B}\right) \exp\left[-j2\pi f \frac{4N_k v_{ab} t_m}{c}\right] \\
&\quad \times \exp\left[-j2\pi\left(\frac{f+f_c}{f_c}\right)\frac{4R_{0k}+4v_{0k}t_m}{\lambda}\right]\delta\left(f_{\tau m}-\frac{2a_k}{\lambda}\right) \\
&\quad + \sum_{i=1}^{K}\sum_{j=i+1}^{K} C_{1-cross,i,j}^*\left(f, t_m, f_{\tau m}\right)
\end{aligned} \tag{15}
$$

This problem is similar to the velocity ambiguity mentioned in [7], [29], and [36]. In order to guarantee the subsequent integration, the first exponential term in (15) must be removed. Define a matched filtering function

$$
H_n\left(f, t_m\right) = \exp\left(j2\pi f \frac{4n v_{ab}}{c} t_m\right) \tag{16}
$$

When $n = N_k$, multiplying $H_{N_k}\left(f, t_m\right)$ with $C_1^*\left(f, t_m, f_{\tau m}\right)$, one has

$$
\begin{aligned}
&C_{1-N_k}^*\left(f, t_m, f_{\tau m}\right) = C_1^*\left(f, t_m, f_{\tau m}\right) H_{N_k}\left(f, t_m\right) \\
&= A_{4k}\, rect\left(\frac{f}{B}\right)\exp\left[-j2\pi\left(\frac{f+f_c}{f_c}\right)\frac{4R_{0k}+4v_{0k}t_m}{\lambda}\right]\delta\left(f_{\tau m}-\frac{2a_k}{\lambda}\right) \\
&\quad + C_{1-N_k-others}^*\left(f, t_m, f_{\tau m}\right)+\sum_{i=1}^{K}\sum_{j=i+1}^{K} C_{1-N_k-cross,i,j}^*\left(f, t_m, f_{\tau m}\right)
\end{aligned} \tag{17}
$$

where, $C_{1-N_k-cross,i,j}^*\left(f, t_m, f_{\tau m}\right)$ denotes the cross-term.

where

$$
\begin{aligned}
&C_{1-N_k-others}^*(f, t_m, f_{\tau m}) \\
&= \sum_{l=1,l\neq k}^{K} A_{4l}\, rect\left(\frac{f}{B}\right)\exp\left[-j2\pi f\frac{4\left(N_l-N_k\right)v_{ab}t_m}{c}\right] \\
&\quad \times \exp\left[-j2\pi\left(\frac{f+f_c}{f_c}\right)\frac{4R_{0l}+4v_{0l}t_m}{\lambda}\right]\delta\left(f_{\tau m}-\frac{2a_l}{\lambda}\right)
\end{aligned} \tag{18}
$$

Thereafter, the 2nd coherent integration along t_m-axis is achieved via scaled inverse FT (SIFT).

$$
\begin{aligned}
&C_{2-N_k}\left(f, f_{tm}, f_{\tau m}\right) \\
&= \int C_{1-N_k}^*\left(f, t_m, f_{\tau m}\right)\exp\left[j2\pi\left(\frac{f+f_c}{f_c}\right)f_{tm}t_m\right]dt_m \\
&= A_{5k}\, rect\left(\frac{f}{B}\right)\exp\left[-j2\pi\left(f+f_c\right)\frac{4R_{0k}}{c}\right] \\
&\quad \times \delta\left(f_{\tau m}-\frac{2a_k}{\lambda}\right)\delta\left(f_{tm}-\frac{4v_{0k}}{\lambda}\right) \\
&\quad + C_{2-N_k-others}\left(f, f_{tm}, f_{\tau m}\right) \\
&\quad + \sum_{i=1}^{K}\sum_{j=i+1}^{K} C_{2-N_k-cross,i,j}\left(f, f_{tm}, f_{\tau m}\right)
\end{aligned} \tag{19}
$$

where f_{tm} denotes the scaled Doppler frequency variable, $A_{5\,k}$ denotes the amplitude, $C_{2-N_k-cross,i,j}\left(f, f_{tm}, f_{\tau m}\right)$ denotes the cross-term.

where

$$
\begin{aligned}
&C_{2-N_k-others}(f, f_{tm}, f_{\tau m}) \\
&= \sum_{l=1,l\neq k}^{K} A_{5l}\, rect\left(\frac{f}{B}\right)\exp\left[-j2\pi\left(f+f_c\right)\frac{4R_{0l}}{c}\right]\delta\left(f_{\tau m}-\frac{2a_l}{\lambda}\right) \\
&\quad \times \delta\left(\frac{f+f_c}{f_c}\left(\frac{4v_{0l}}{\lambda}-f_{tm}\right)+f\frac{4\left(N_l-N_k\right)v_{ab}}{c}\right)
\end{aligned} \tag{20}
$$

It can be observed from (19) that the energy of the k-th auto-term is concentrated along a line parallel to f- axis. Thus, the final coherent integration along f-axis is achieved via inverse FT (IFT), after which the TDCI domain is obtained as expressed in (21). Due to the 2nd Dirac delta function in (20), the fold uncompensated auto-terms cannot be integrated by the final integration.

$$
\begin{aligned}
&TDCI_{N_k}\left(t', f_{tm}, f_{\tau m}\right) \\
&= \int C_{2-N_k}\left(f, f_{tm}, f_{\tau m}\right)\exp\left(j2\pi ft'\right)df \\
&= A_{6k}\exp\left(-j2\pi\frac{4R_{0k}}{\lambda}\right)\delta\left(f_{\tau m}-\frac{2a_k}{\lambda}\right)\delta\left(f_{tm}-\frac{4v_{0k}}{\lambda}\right) \\
&\quad \times \sin c\left[B\left(t'-\frac{4R_{0k}}{c}\right)\right] + TDCI_{N_k-others}\left(t', f_{tm}, f_{\tau m}\right) \\
&\quad + \sum_{i=1}^{K}\sum_{j=i+1}^{K} TDCI_{N_k-cross,i,j}\left(t', f_{tm}, f_{\tau m}\right)
\end{aligned} \tag{21}
$$

where, t' denotes the new fast time variable, $A_{6\,k}$ denotes the amplitude, $TDCI_{N_k-others}\left(t', f_{tm}, f_{\tau m}\right)$ denotes the fold uncompensated auto-terms, $TDCI_{N_k-cross,i,j}\left(t', f_{tm}, f_{\tau m}\right)$ denotes the cross-term.

Equation (21) indicates that the energy of the k-th target signal is coherently integrated into a point $\left(4R_{0k}/c, 4v_{0k}/\lambda, 2a_k/\lambda\right)$ in TDCI domain. According to the point, the motion parameters can be accurately estimated. Fig. 1 shows the diagram of TDCI algorithm, where the dark shadings represent the energy of the target signal.

The formulation of TDCI algorithm is summarized as

$$
\begin{aligned}
&TDCI_n\left(t', f_{tm}, f_{\tau m}\right) \\
&= \int\int\int s_f\left[f, t_m+\left(\tau_m+\frac{h}{2}\right)\right] \\
&\quad \cdot s_f\left[f, t_m-\left(\tau_m+\frac{h}{2}\right)\right]H_n\left(f, t_m\right) \\
&\quad \times \exp\left\{j2\pi\left(\frac{f+f_c}{f_c}\right)f_{\tau m}\left[\left(\tau_m+\frac{h}{2}\right)^2+t_m^2\right]\right\} \\
&\quad \times \exp\left[j2\pi\left(\frac{f+f_c}{f_c}\right)f_{tm}t_m\right]\exp\left(j2\pi ft'\right)d\tau_m dt_m df
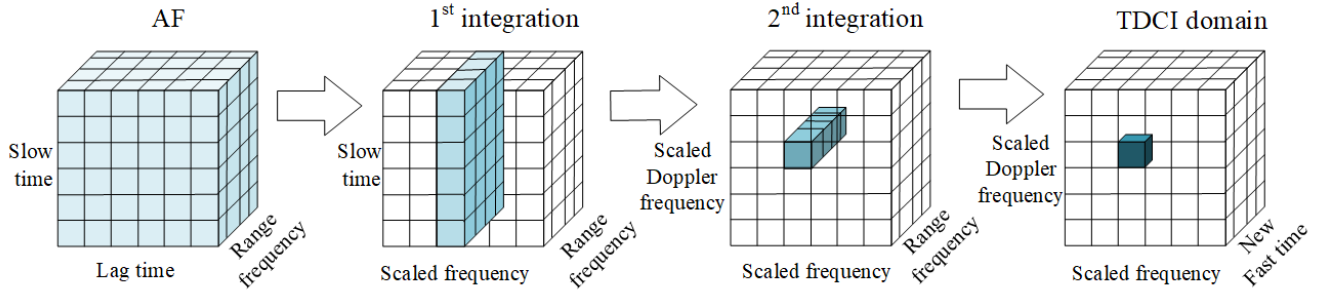\end{aligned} \tag{22}
$$

FIGURE 1. Diagram of TDCI algorithm.

B. TDCI BASED DETECTION ALGORITHM

According to the principle in Section III-A, the motion parameters can be accurately estimated by TDCI algorithm. Based on that, we propose a novel detection algorithm. Next, the main procedure is given.

Step 1. Transform the signal $s_{pc}(t, t_m)$ by TDCI algorithm with all possible autocorrelation fold factors and acquire the transformation result $TDCI_n(t', f_{tm}, f_{\tau m})$.

Step 2. Estimate the radial velocity and acceleration (i.e. $\hat{v}_i$ and $\hat{a}_i$) by the highest peak.

$$\left\{\hat{v}_i = \frac{f_{tm}\lambda}{4} + nv_{ab}, \hat{a}_i = \frac{f_{\tau m}\lambda}{2}\right\}$$
$$= \arg\max_{n, f_{tm}, f_{\tau m}} \left\{TDCI_n\left(t', f_{tm}, f_{\tau m}\right)\right\} \quad (23)$$

Step 3. Compensate the RCM and DFM by $\hat{v}_i$ and $\hat{a}_i$.

$$s_{com}(f, t_m)$$
$$= s_f(f, t_m) \exp\left(j\frac{2\pi}{c}(f + f_c)\hat{a}_i t_m^2\right) \exp\left(j\frac{4\pi}{c}f\hat{v}_i t_m\right) \quad (24)$$

Then transform the signal into range-Doppler frequency domain, expressed as

$$S_{Doppler}(t, f_d) = \mathrm{FT}_{tm}\left\{\mathrm{IFT}_f\left[s_{com}(f, t_m)\right]\right\} \quad (25)$$

where f_d denotes the Doppler frequency variable. FT and IFT denote the FT and IFT operators, respectively.

Thereafter, realize CFAR detection in range-Doppler frequency domain and obtain the estimations for the initial radial range and the amplitude (i.e. $\hat{R}_{0i}$ and $\hat{A}_{2i}$)

$$\hat{R}_{0i} = \frac{ct_{de}}{2} \quad (26)$$

$$\hat{A}_{2i} = \frac{\left|S_{Doppler}(t_{de}, f_{de})\right|}{M} \quad (27)$$

where (t_{de}, f_{de}) denotes the coordinate of the detected target, M denotes the pulse number.

Step 4. CLEAN the detected target.

Similar to the illustration in [37], while the differences among the energies of the targets signals are large, the weak targets may be submerged by the strong ones and noise in TDCI domain, which is so-called shadow effect. In order
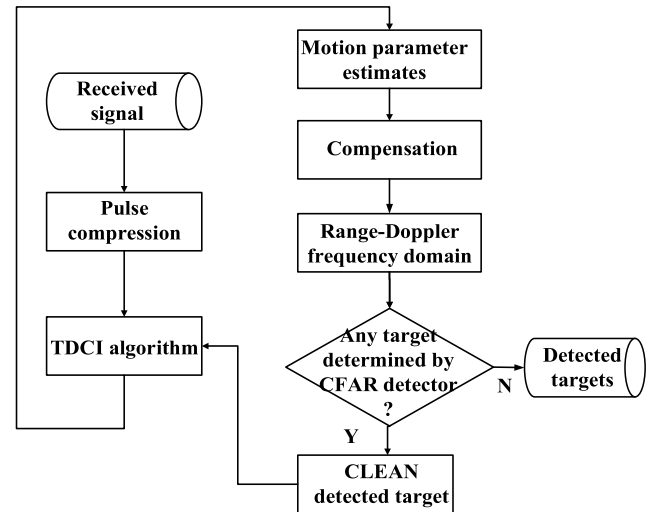

FIGURE 2. Flow chart of the proposed algorithm.

to avoid that, CLEAN algorithm [36] should be employed, expressed as,

$$s_{pc}(t, t_m) = s_{pc}(t, t_m) - \hat{A}_{2i}\operatorname{sinc}\left[B\left(t - \frac{2\hat{R}_{0i} + 2\hat{v}_i t_m + \hat{a}_i t_m^2}{c}\right)\right]$$
$$\times \exp\left(-j2\pi f_c\frac{2\hat{R}_{0i} + 2\hat{v}_i t_m + \hat{a}_i t_m^2}{c}\right) \quad (28)$$

Step 5. Repeat Step 1 to Step 4 until no target can be detected.

By the iteration, all the targets can be detected. The flow chart of the proposed algorithm is shown in Fig. 2.

IV. ANALYSES OF THE PROPOSED ALGORITHM

The principle of the proposed algorithm is given detailedly in Section III. In this section, five aspects are discussed in theory and verified by simulations, including integration capability, cross-term suppression, resolution, efficient implementation and computation complexity.

A. INTEGRATION CAPABILITY

According to the principle, the proposed detection algorithm is based on TDCI algorithm. In this part, we demonstrate
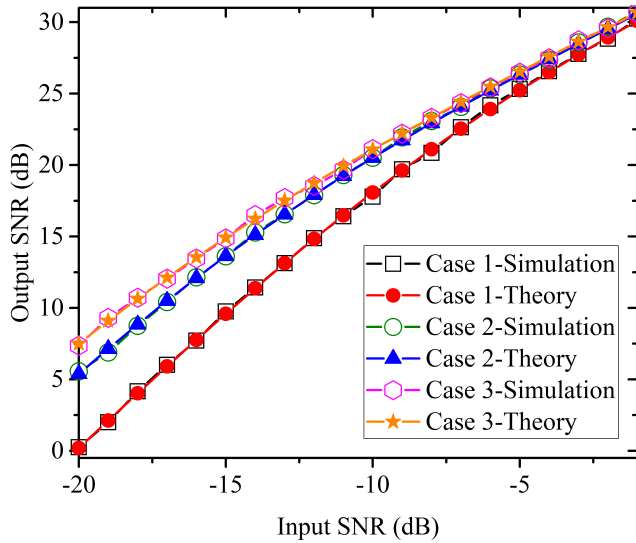
FIGURE 3. Simulation results of Section IV-A.

TABLE 1. Parameters of the simulations.

	Case 1	Case 2	Case 3
Range gate number	400	100	100
Pulse number	100	100	100
Sampling number in the pulse width	30	30	30
Bandwidth (MHz)	30	30	30
Sampling frequency (MHz)	30	30	60

the theoretical integration capability of TDCI algorithm via deriving the relationship between the SNR of the received target signal (i.e. input SNR) and the SNR of the integrated target signal in TDCI domain (i.e. output SNR). The relationship is detailedly derived in Appendix A, expressed as

$$SNR_{out} = \frac{M^2 \frac{F_s \eta^2}{BN} SNR_{in}^2}{2\left(M \frac{F_s \eta}{BN} SNR_{in} + 1\right)} \quad (29)$$

where SNR_{out} and SNR_{in} denote the output and input SNRs, respectively, M, N, and η denote the pulse number, range gate number, and sampling number in the pulse width, respectively, F_s and B denote the sampling frequency and bandwidth, respectively.

In order to prove the correctness of the derivation, three cases are simulated by 1000 Monte Carlo runs. The parameters are listed in Table 1 and the results are shown in Fig. 3. It can be observed that the simulation curves fit the theory curves well, verifying the validity of the derivation process. It is worth noting that in addition to increasing M and η, moderately increasing the ratio of F_s and BN can effectively improve the integration capability in the case of low input SNR, which can be proved by (29) and reflected from the results of Case 1, Case 2, and Case 3.

B. CROSS-TERM ANALYSIS
In multi-target scenario, several cross-terms are generated by the AF as shown in (9) and (10). The effect of the cross-term on the detection performance is derived in Appendix B. According to the analysis, we can draw an important conclusion that the cross-term cannot affect the performance of the proposed algorithm and can be ignored. This conclusion can be proved by the following simulation. The radar parameters and the target motion parameters are given in Table 2. The constant delay h is 1s. The simulation results are shown in Fig. 4.

Fig. 4 (a) gives the PC result of the received signal where five targets appear. As shown in Fig. 4 (b), due to the same velocity and acceleration, a cross-term generated by Target A and B occurs in TDCI domain. Consistent with the theoretical analysis, the velocity and acceleration can be accurately estimated by the integrated cross-term. As displayed in Fig. 4 (c), compensating off the RCM and DFM, Target A and B are integrated and detected in range-Doppler frequency domain simultaneously. According to the proposed algorithm, the two targets are removed by CLEAN algorithm after detection. Fig. 4 (d) to (i) show the detection procedures of Target C to E. The processes are the same as those of Target A and B. Likewise, they are detected successfully one after another in range-Doppler frequency domain. Particularly, in Fig. 4 (b), due to the low SNR, Target E is submerged by the cross-term and noise, that is shadow effect. From the simulation, it is observed that all the targets are detected without the influences of shadow effect and cross-term, which proves the correctness of the analysis and the validity of the proposed algorithm.

C. RESOLUTION ANALYSIS
In Section III, we give the theory of the proposed algorithm. For the finite-time signal, (21) should be written as

$$TDCI_{N_k}\left(t', f_{tm}, f_{\tau m}\right)$$
$$= A_{6k} \exp\left(-j2\pi \frac{4R_{0k}}{\lambda}\right)$$
$$\times \int \exp\left[j2\pi \left(\frac{f+f_c}{f_c}\right)\left(\tau_m + \frac{h}{2}\right)^2\left(f_{\tau m} - \frac{2a_k}{\lambda}\right)\right] d\tau_m$$
$$\times \text{sin} c\left[\frac{T}{2}\left(f_{tm} - \frac{4v_{0k}}{\lambda}\right)\right] \text{sin} c\left[B\left(t' - \frac{4R_{0k}}{c}\right)\right]$$
$$+ TDCI_{N_k-others}\left(t', f_{tm}, f_{\tau m}\right)$$
$$+ \sum_{i=1}^{K}\sum_{j=i+1}^{K} TDCI_{N_k-cross,i,j}\left(t', f_{tm}, f_{\tau m}\right) \quad (30)$$

where T denotes the integration time.

The finite-time TDCI cannot be given in a closed analytical form due to the Fresnel integration transform along τ_m. Fortunately, according to the analysis in [35], the theoretical resolution of acceleration can be acquired. The theoretical resolutions of velocity and acceleration are calculated based on the formula given in (30), expressed as

$$R_v = \frac{\lambda}{2T} \quad (31)$$
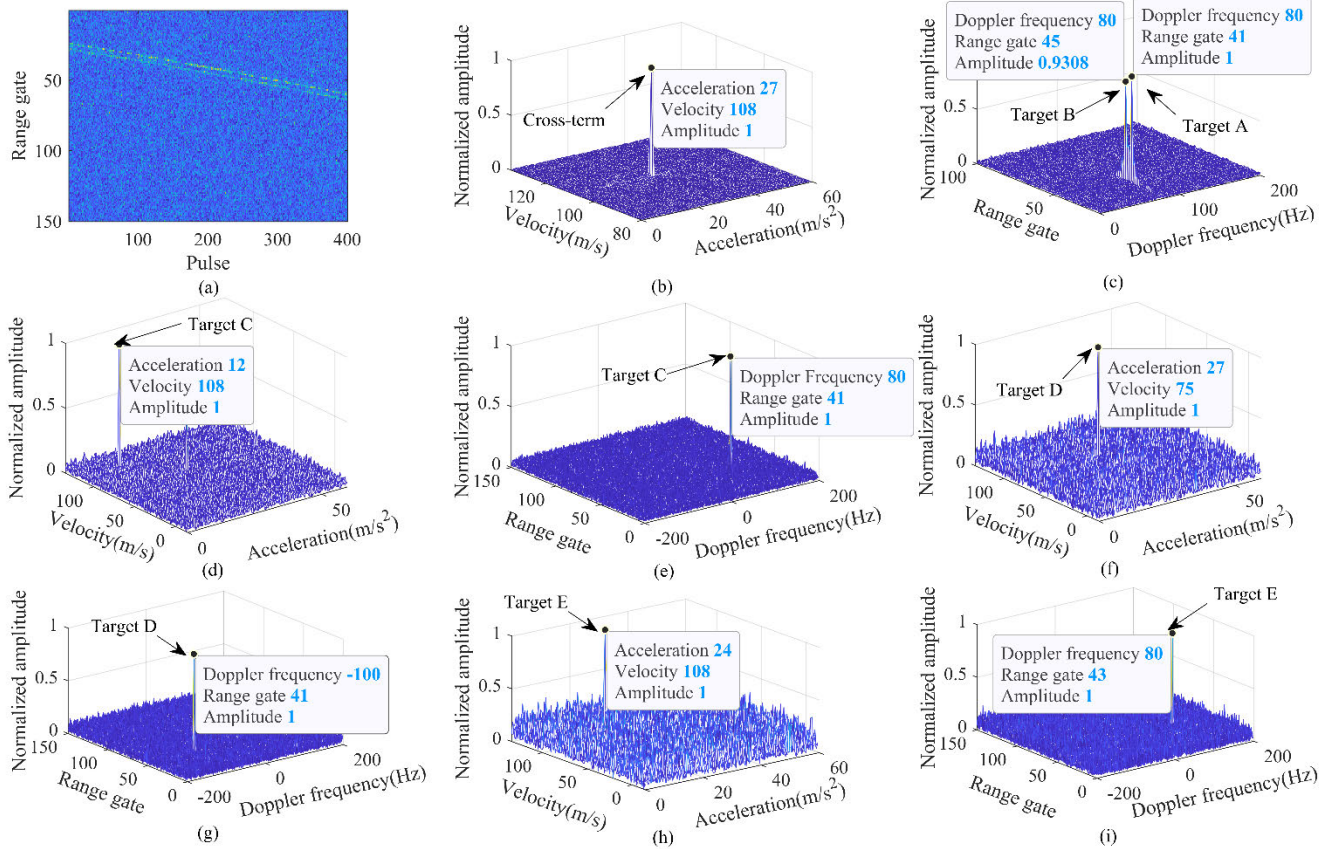
FIGURE 4. Simulation results of Section IV-B. (a) Received radar signal after PC. (b) Integrated cross-term in TDCI domain. (c) Integrated Target A and Target B in range-Doppler frequency domain. (d) Integrated Target C in TDCI domain. (e) Integrated Target C in range-Doppler frequency domain. (f) Integrated Target D in TDCI domain. (g) Integrated Target D in range-Doppler frequency domain. (h) Integrated Target E in TDCI domain. (i) Integrated Target E in range-Doppler frequency domain.

TABLE 2. Radar parameters and target motion parameters.

		Sampling frequency (MHz)	50
Carrier frequency (GHz)	1		
Bandwidth (MHz)	40	Pulse number	400
PRF (Hz)	400	Pulse width (μs)	0.6
	Initial range gate	Velocity (m/s)	Acceleration (m/s²)	Input SNR (dB)
---	---	---	---	---
Target A	41	108	27	-10
Target B	45	108	27	-10
Target C	41	108	12	-15
Target D	41	75	27	-18
Target E	43	108	24	-21

TABLE 3. Radar parameters and target motion parameters.

		Sampling frequency (MHz)	60
Carrier frequency (GHz)	1		
Bandwidth (MHz)	30	Pulse number	100
PRF (Hz)	100	Pulse width (μs)	0.5
	Initial range (m)	Velocity (m/s)	Acceleration (m/s²)	Input SNR (dB)
---	---	---	---	---
Target 1	1200	30	7.5	-10
Target 2	1200	30.15	7.5	-10
Target 3	1200	30	7.8	-10
Target 4	1205	30	7.5	-10

$$R_a = \frac{4\lambda}{(T+h)^2} \tag{32}$$

As illustrated in Section IV-B, affected by the cross-term, targets with the same velocity and acceleration should be distinguished in range-Doppler frequency domain where the range resolution is expressed as

$$R_r = \frac{c}{2B} \tag{33}$$

Below, four point targets denoted as Target 1 to 4 are simulated. The radar parameters are listed in Table 3. The constant delay h is 1s. According to the parameters, the theoretical

resolutions of range, velocity, and acceleration are 5 m, 0.15 m/s, and 0.3 m/s², respectively. Based on these values, the target motion parameters are set. As shown in Fig. 5, Target 2 to 4 can be effectively distinguished with Target 1, which verifies the correctness of the analysis and the effectiveness of the proposed algorithm.

D. NUFFT & CHIRP-Z BASED IMPLEMENTATION
The discrete form of $R(f, t_m, \tau_m)$ is expressed as

$$R(n, m, l) = s_f\left[n, m + \left(l + \frac{h}{2}F_P\right)\right] s_f\left[n, m - \left(l + \frac{h}{2}F_p\right)\right] \tag{34}$$
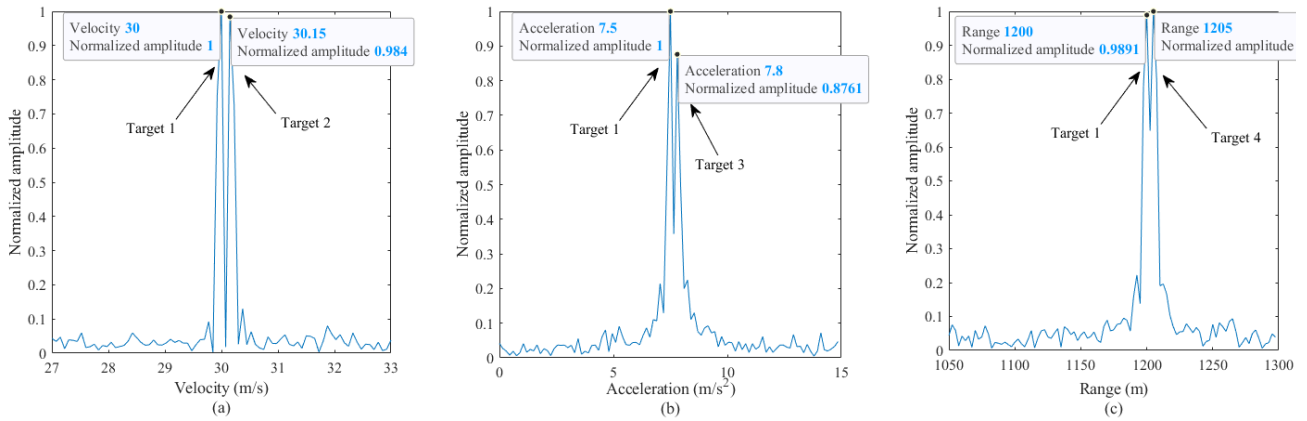
FIGURE 5. Simulation results of Section IV-C. (a) Simulation results of Target 1 and Target 2. (b) Simulation results of Target 1 and Target 3. (c) Simulation results of Target 1 and Target 4.

where

$$n = [-N/2], \quad [-N/2] + 1 \ldots [N/2] - 1,$$
$$m = [-M/2], \quad [-M/2] + 1 \ldots [M/2] - 1,$$
$$l = [-M/2], \quad [-M/2] + 1 \ldots [M/2] - 1$$

where F_P denotes the pulse repetition frequency.

By performing the 1st coherent integration, we obtain

$$C_1(n, m, r) = \sum_l R(n, m, l) \exp\left[j2\pi r \frac{n\frac{Fs}{N} + f_c}{f_c} \left(\frac{l}{F_P} + \frac{h}{2} \right)^2 \right] \tag{35}$$

where F_s denotes the sampling frequency.

This process can be effectively implemented and sped up via non-uniform fast FT (NUFFT) [31], [32], which can be expressed as

$$C_1(n, m, r) = \text{NUFFT}_l[R(n, m, l)] \tag{36}$$

where NUFFT$_l$ denotes the NUFFT operation with respect to l.

The discrete decoupling matrix and matched filtering matrix are given as follow,

$$D = \exp\left[j2\pi r \frac{n\frac{Fs}{N} + f_c}{f_c} \left(\frac{m}{F_P} \right)^2 \right] \tag{37}$$

$$H_{N_k} = \exp\left[j2\pi n \frac{Fs}{N} \frac{4N_k v_{ab}}{c} \left(\frac{m}{F_P} \right) \right] \tag{38}$$

Compensating off $C_1(n, m, r)$ by D and H_{N_k}, we obtain,

$$C_{1-N_k}^*(n, m, r) = C_1(n, m, r) D H_{N_k} \tag{39}$$

Afterwards, the 2nd coherent integration can be achieved, expressed as

$$C_{2-N_k}(n, p, r)$$
$$= \sum_m C_{1-N_k}^*(n, m, r) \exp\left[j2\pi p \frac{n\frac{Fs}{N} + f_c}{f_c} \left(\frac{m}{F_P} \right) \right] \tag{40}$$

This process can be effectively implemented and sped up via chirp-z transform (CZT) [31], [32], which can be expressed as

$$C_{2-N_k}(n, p, r) = \text{CZT}_m\left[C_{1-N_k}^*(n, m, r) \right] \tag{41}$$

where CZT$_m$ denotes the CZT operation with respect to m.

Finally, performing inverse fast FT (IFFT), we obtain TDCI

$$TDCI_{N_k}(q, p, r) = \text{IFFT}_n\left[C_{2-N_k}(n, p, r) \right] \tag{42}$$

where IFFT$_n$ denotes the IFFT operation with respect to n.

Basing on (34)-(42), we give the brief expression of NUFFT & chirp-z based implementation for TDCI.

$$TDCI_{N_k}(q, p, r)$$
$$= \text{IFFT}_n\left[\text{CZT}_m\left[\text{NUFFT}_l\left[R(n, m, l) \right] D H_{N_k} \right] \right] \tag{43}$$

E. COMPUTATION COMPLEXITY

Denote the numbers of range gates, echo pulses, searching autocorrelation fold factors by N, M, and N_s, respectively. As to the proposed algorithm, the main procedure includes: AF with its computation cost being $[O(M^2 N)]$, 1st coherent integration by NUFFT $[O(M^2 N \log_2 M)]$, decoupling operation $[O(M^2 N)]$, velocity compensation $[O(N_s M^2 N)]$, 2nd coherent integration by CZT $[O(N_s M^2 N \log_2 M)]$, final coherent integration by IFFT $[O(N_s M^2 N \log_2 N)]$, parameters compensation and coherent integration in range-Doppler frequency domain $(O[MN + MN(\log_2 N + \log_2 M)])$. Thus, the overall computation cost of the proposed algorithm can be approximately calculated in the order of $O[M^2 N N_s (\log_2 M + \log_2 N)]$.

In this subsection, the computation complexities of GRFT and TDST are given for comparison. In order to achieve a reasonable comparison, we consider the same parameter range and estimation accuracy for the three algorithms. Under this circumstance, the numbers of searching velocity and acceleration by GRFT should be set MN_s and M, respectively. According to [27] and [28], the computation complexity

TABLE 4. Computation complexities.

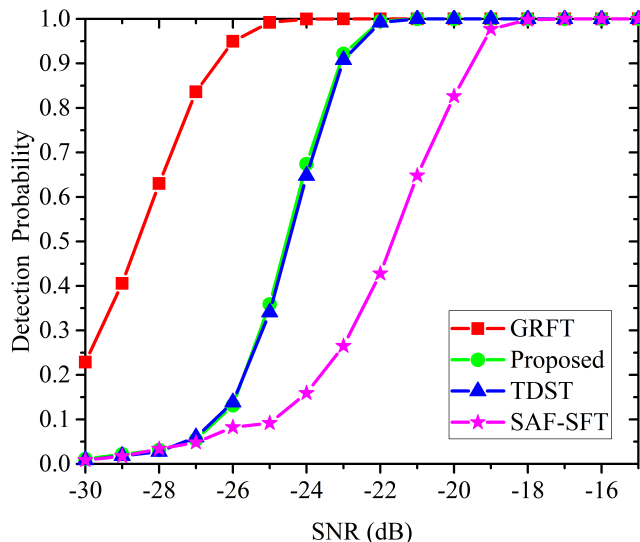| Algorithm	Computation complexity
GRFT	$O(M^3NN_s)$
Proposed	$O[M^2NN_s(log_2M+log_2N)]$
TDST	$O[M^3N_s(log_2MN_s+log_2M)]$

FIGURE 6. Detection probability curves.

TABLE 5. Radar parameters and target motion parameters.

Carrier frequency (GHz)	1	Sampling frequency (MHz)	62.5
Bandwidth (MHz)	30	Pulse number	256
PRF (Hz)	256	Pulse width (μs)	0.64

	Initial range gate	Velocity (m/s)	Acceleration (m/s²)	Input SNR (dB)
Target	41	72	9	-30~-15

of GRFT can be approximately calculated in the order of $O(M^3NN_s)$. Considering the same parameter range and estimation accuracy, the size of the domain by TDST algorithm should be expanded to MN_s (*velocity*) $\times M$ (*acceleration*) $\times M$ (*baseband velocity*). According to [30], the computation complexity of TDST can be approximately calculated in the order of $O[M^3N_s(log_2MN_s + log_2M)]$.

Table 4 lists the computation complexities of the three algorithms. It can be observed that under the same condition, the proposed algorithm requires the least computation cost.

V. NUMERICAL EXPERIMENTS

This section is devoted to evaluate the performance of the proposed algorithm where simulated and real data are processed. Moreover, several comparisons are carried out.

A. DETECTION CAPABILITY

In this subsection, the detection probabilities of a point target by GRFT, the proposed algorithm, TDST, and SAF-SFT are compared via 500 Monte Carlo runs. The radar parameters
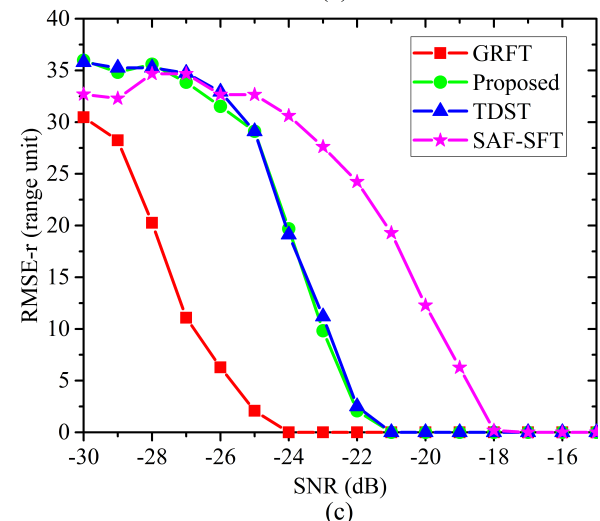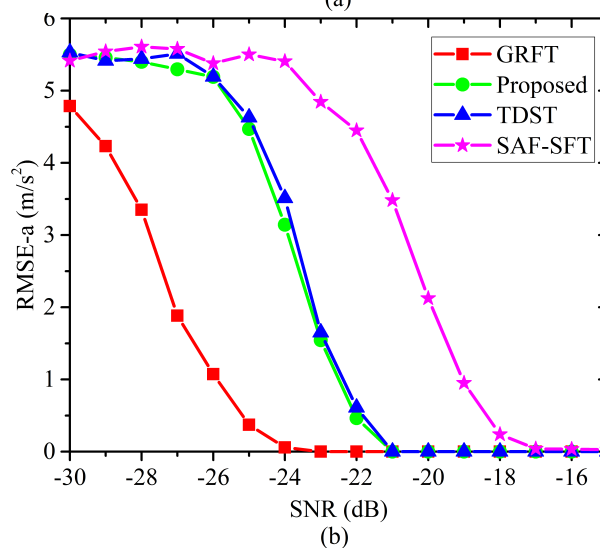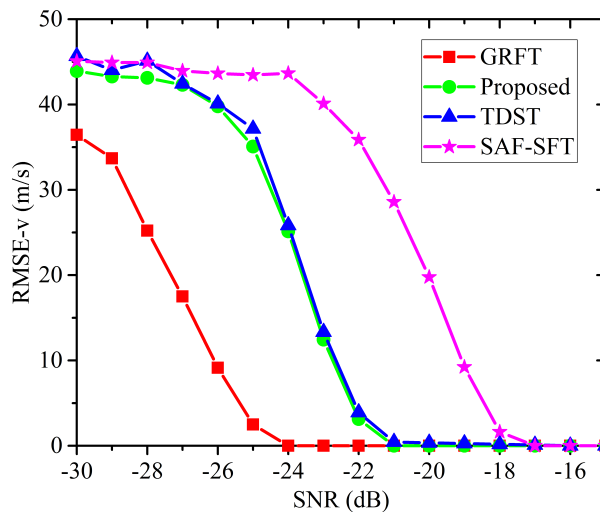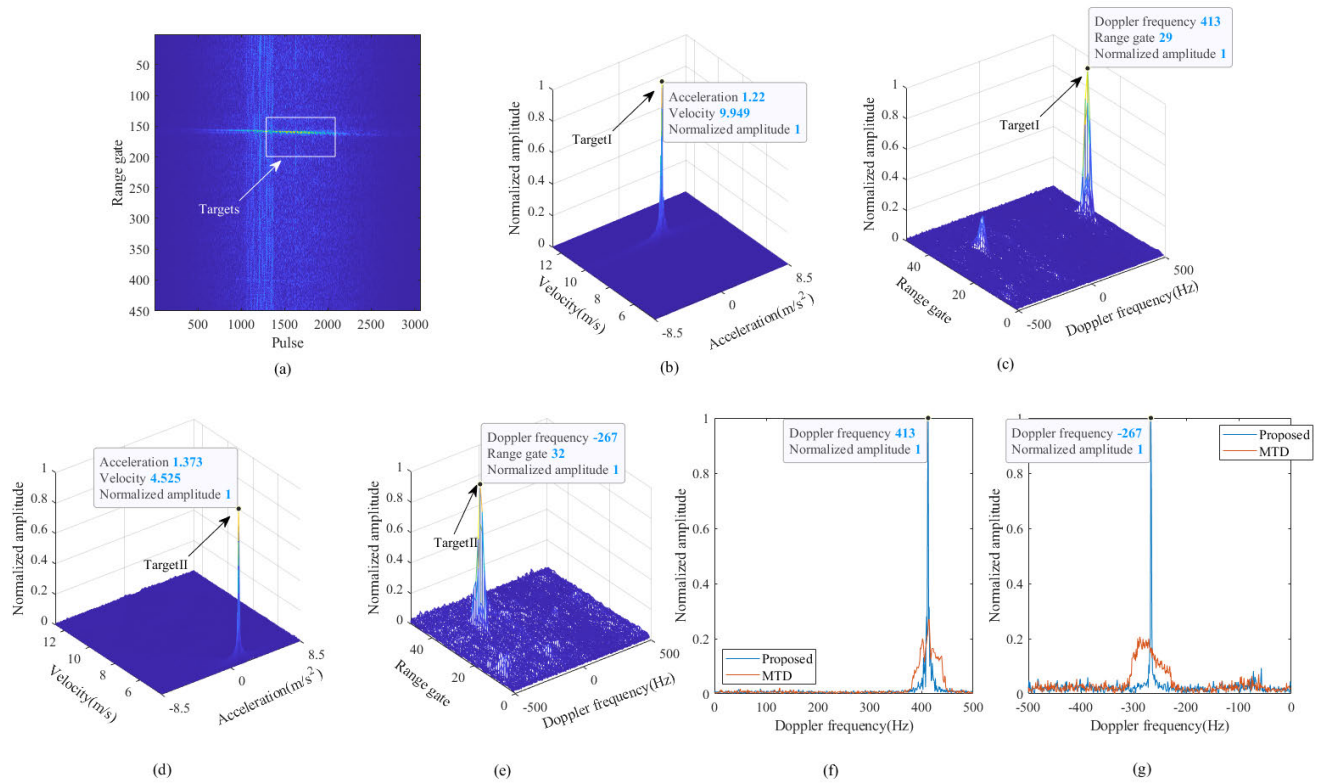

FIGURE 7. RMSE curves. (a) RMSEs of velocity estimates. (b) RMSEs of acceleration estimates. (c) RMSEs of range unit estimates.

and target motion parameters are listed in Table 5. The constant delay h is set as 1s. The false alarm probability is set as 10^{-6}. The detection probability curves are shown in Fig. 6.

FIGURE 8. Processing results of the real data. (a) Received data after PC. (b) Integrated Target I in TDCI domain. (c) Integrated Target I in range-Doppler frequency domain. (d) Integrated Target II in TDCI domain. (e) Integrated Target II in range-Doppler frequency domain. (f) Integration results of Target I by the proposed algorithm and MTD. (g) Integration results of Target II by the proposed algorithm and MTD.

For the detection probability $P_d = 0.9$, the required SNR of the proposed algorithm is about 3 dB higher than that of GRFT, which is induced by the AF. Accordingly, it asks for much lower computation cost as illustrated in Section IV-E. It can be observed that the proposed algorithm has almost the same detection performance as TDST. However, its computation burden is much lighter. SAF-SFT algorithm cannot perform as well as the other three algorithms. That is due to the application of SAF.

B. PARAMETER ESTIMATION ACCURACY

In this subsection, the parameter estimation accuracy of a point target by GRFT, the proposed algorithm, TDST, and SAF-SFT are compared via 500 Monte Carlo runs. The root mean square error (RMSE) is introduced as an evaluation criterion. The radar parameters and the target motion parameters are the same as those of the simulation in Section V-A. The RMSE curves are shown in Fig. 7.

Obviously, thanks to the 3-D searching process, GRFT has the most superior performance. Accordingly, it requires the highest computation complexity as illustrated in Section IV-E. The performances of TDST and the proposed algorithm are approximately the same. The difference is that the proposed algorithm asks for much lower computation complexity. Compared with the proposed algorithm,

SAF-SFT algorithm suffers from 4 dB SNR loss. That is brought about by the SAF operation.

Combining the results of Section V-A, B, and Section IV-E, we conclude that the proposed algorithm can strike a good balance between computation complexity and anti-noise performance. It can be a good candidate for maneuvering target detection and parameter estimation.

C. REAL DATA

In this subsection, a set of real measured data is processed to verify the validity of the proposed algorithm. The real data is obtained by an outfield experiment near the airport in Xi'an, China. The data is recorded by an airborne X-band radar whose parameters are listed in Table 6. Two cooperative cars denoted as Target I and Target II are tested. The processing results are shown in Fig. 8.

As shown in Fig. 8 (a), after clutter suppression, one bright band appears covering the two targets. 500 pulses are selected for target detection in this experiment. The constant delay h is 0.5s. As described in Fig. 8 (b) to (e), by the proposed algorithm, the two targets are detected successfully one by one with their parameters estimated accurately. Comparing with the motion parameters given by the vehicle satellite navigation receivers, we confirm correctness of the detection. Fig. 8 (f) and (g) show the integration results of the two targets in range-Doppler frequency domain by the proposed

TABLE 6. Radar parameters of the real data.

Parameters	value
Carrier frequency (GHz)	8.85
Bandwidth (MHz)	40
Sampling frequency (MHz)	60
Velocity of platform (m/s)	120
Pulse repetition frequency (Hz)	1000
Nearest slant-range (m)	9000

TABLE 7. Output SNRs by the proposed algorithm and GRFT.

	Proposed	GRFT
Target I	42.47 dB	42.47 dB
Target II	34.27 dB	34.27 dB

algorithm and MTD. Obviously, the proposed algorithm outperforms MTD. The difference between the peaks is caused by the uncompensated DFM. Besides, the output SNRs by the proposed algorithm and GRFT are listed in Table 7. It can be observed that for these data, the proposed algorithm reaches the same detection performance as GRFT with lower computation cost. The processing and result analysis above demonstrate the validity of the proposed algorithm. And it is appropriate for the maneuvering target detection and parameter estimation.

VI. CONCLUSION

In this article, a novel TDCI based algorithm is proposed for the maneuvering target detection and parameter estimation. Based on mathematical analyses and numerical simulations, the advantages of the proposed algorithm are summarized as follow: 1) it can effectively eliminate RCM and DFM; 2) it can effectively cope with the problems of velocity ambiguity, shadow effect, and cross-term with superior resolution; 3) compared with several existing algorithms, it strikes a good balance between computation complexity and anti-noise performance. Moreover, real data processing and result analysis further verify the effectiveness of the proposed algorithm.

APPENDIX A

Motivated by the reference [38] to [40], we calculate the output SNR by the discrete form of TDCI algorithm. For the conciseness, we consider the mono-target scenario. Define the discrete form of the received noisy target signal as $S_r(n, m)$ whose SNR is expressed as

$$SNR_{in} = \frac{A_r^2}{\sigma_r^2} \tag{44}$$

where A_r denotes the amplitude of the clean target signal, σ_r^2 denotes the variance of the noise.

By PC, we obtain the discrete form of the noisy signal in range frequency domain, expressed as

$$S_f(n, m) = s_f(n, m) + x(n, m) \tag{45}$$

where $s_f(n, m)$ denotes the clean target signal, $x(n, m)$ denotes the additive zero-mean Gauss white noise.

According to the stationary phase principle, in this domain, the SNR is expressed as

$$SNR_f = \frac{A^2}{\sigma^2} = \frac{F_s \eta}{BN} SNR_{in} \tag{46}$$

where A denotes the amplitude of the clean target signal, σ^2 denotes the variance of the noise, F_s denotes the sampling frequency, η denotes the sampling number in the pulse width, B denotes the bandwidth, N denotes the range gate number.

According to Section IV-D, regardless of the velocity compensation, the discrete noisy target signal by TDCI can be expressed as

$TDCI(q, p, r)$
$$= \sum_n \sum_m \sum_l S_f \left[n, m + \left(l + \frac{h}{2} F_P\right)\right] S_f \left[n, m - \left(l + \frac{h}{2} F_p\right)\right]$$
$$\times \exp\left\{j2\pi \frac{n\frac{Fs}{N} + f_c}{f_c} \left[r \left(\left(\frac{l}{F_P} + \frac{h}{2}\right)^2 + \left(\frac{m}{F_P}\right)^2\right) + p\left(\frac{m}{F_P}\right)\right]\right\}$$
$$\times \exp\left(j2\pi qn \frac{F_s}{N}\right) \tag{47}$$

Suppose the target signal is theoretically integrated at (q_r, p_v, r_a) in TDCI domain, the output SNR can be defined as

$$SNR_{out} = \frac{|TDCI_c(q_r, p_v, r_a)|^2}{var[TDCI(q_r, p_v, r_a)]} \tag{48}$$

where $TDCI_c(q_r, p_v, r_a)$ and $TDCI(q_r, p_v, r_a)$ denote the clean target signal and the noisy target signal by TDCI algorithm, respectively.

$TDCI_c(q_r, p_v, r_a)$ in (48) can be easily calculated, represented as

$$TDCI_c(q_r, p_v, r_a) = \frac{BM^2 A^2 N}{2F_s} \tag{49}$$

where M denotes the pulse number.

var$[TDCI(q_r, p_v, r_a)]$ in (48) can be obtained by the following relationship, expressed as

var$[TDCI(q_r, p_v, r_a)]$
$$= E[TDCI(q_r, p_v, r_a)^2] - E[TDCI(q_r, p_v, r_a)]^2 \tag{50}$$

Similar to (49), $E[TDCI(q_r, p_v, r_a)]$ in (50) can be easily acquired, expressed as

$$E[TDCI(q_r, p_v, r_a)] = \frac{BM^2 A^2 N}{2F_s} \tag{51}$$

Let

$$s_1 = s_f(n_1, m_1 + l_1 + 0.5\, hF_p),$$
$$s_2 = s_f(n_1, m_1 - l_1 - 0.5\, hF_p),$$
$$s_3 = s_f(n_2, m_2 + l_2 + 0.5\, hF_p),$$
$$s_4 = s_f(n_2, m_2 - l_2 - 0.5\, hF_p),$$
$$x_1 = x(n_1, m_1 + l_1 + 0.5\, hF_p),$$
$$x_2 = x(n_1, m_1 - l_1 - 0.5\, hF_p),$$
$$x_3 = x(n_2, m_2 + l_2 + 0.5\, hF_p),$$

$$x_4 = x(n_2, m_2 - l_2 - 0.5 \, hF_p),$$

and

$$
\begin{aligned}
&\varphi(n_1, m_1, l_1, n_2, m_2, l_2)\\
&= \frac{r_a}{f_c} \left\{ \begin{array}{l}
\left(n_1 \frac{Fs}{N} + f_c\right)\left[\left(\frac{l_1}{F_P} + \frac{h}{2}\right)^2 + \left(\frac{m_1}{F_P}\right)^2\right]\\
- \left(n_2 \frac{Fs}{N} + f_c\right)\left[\left(\frac{l_2}{F_P} + \frac{h}{2}\right)^2 + \left(\frac{m_2}{F_P}\right)^2\right]
\end{array} \right\}\\
&\quad + \frac{p_v}{f_c}\left[\left(n_1 \frac{Fs}{N} + f_c\right)\frac{m_1}{F_P} - \left(n_2 \frac{Fs}{N} + f_c\right)\frac{m_2}{F_P}\right]\\
&\quad + q_r \frac{F_s}{N}(n_1 - n_2)
\end{aligned}
$$

Then, the second-order moment $E[TDCI(q_r, p_v, r_a)^2]$ in (50) can be calculated as

$$
\begin{aligned}
&E[TDCI(q_r, p_v, r_a)^2]\\
&= E\Big\{ \sum_{n_2}\sum_{m_2}\sum_{l_2}\sum_{n_1}\sum_{m_1}\sum_{l_1}(s_1 + x_1)(s_2 + x_2)\\
&\qquad \times (s_3^* + x_3^*)(s_4^* + x_4^*)\\
&\qquad \times \exp[j2\pi\varphi(n_1, m_1, l_1, n_2, m_2, l_2)]\Big\}\\
&= \sum_{n_2}\sum_{m_2}\sum_{l_2}\sum_{n_1}\sum_{m_1}\sum_{l_1}\\
&\quad \times \left[\begin{array}{l}
s_1 s_2 s_3^* s_4^*\\
+ s_1 s_3^* E\left\{x_2 x_4^*\right\} + s_2 s_3^* E\left\{x_1 x_4^*\right\}\\
+ s_1 s_4^* E\left\{x_2 x_3^*\right\} + s_2 s_4^* E\left\{x_1 x_3^*\right\}\\
+ E\left\{x_1 x_3^*\right\} E\left\{x_2 x_4^*\right\} + E\left\{x_1 x_4^*\right\} E\left\{x_2 x_3^*\right\}
\end{array}\right]\\
&\quad \times \exp[j2\pi\varphi(n_1, m_1, l_1, n_2, m_2, l_2)]\Big\} \qquad (52)
\end{aligned}
$$

The parts in the summation can be calculated by

$$
\begin{aligned}
s_1 s_2 s_3^* s_4^* &= A^4\\
s_1 s_3^* E\left\{x_2 x_4^*\right\} &= A^2\sigma^2\delta(n_1 - n_2)\delta(m_1 - l_1 - m_2 + l_2)\\
s_2 s_3^* E\left\{x_1 x_4^*\right\} &= A^2\sigma^2\delta(n_1 - n_2)\delta(m_1 + l_1 - m_2 + l_2 + hF_P)\\
s_1 s_4^* E\left\{x_2 x_3^*\right\} &= A^2\sigma^2\delta(n_1 - n_2)\delta(m_1 - l_1 - m_2 - l_2 - hF_P)\\
s_2 s_4^* E\left\{x_1 x_3^*\right\} &= A^2\sigma^2\delta(n_1 - n_2)\delta(m_1 + l_1 - m_2 - l_2)\\
E\left\{x_1 x_3^*\right\}&E\left\{x_2 x_4^*\right\}\\
&= \sigma^4\delta(n_1 - n_2)\delta(m_1 + l_1 - m_2 - l_2)\delta(m_1 - l_1 - m_2 + l_2)\\
E\left\{x_1 x_4^*\right\}&E\left\{x_2 x_3^*\right\}\\
&= \sigma^4\delta(n_1 - n_2)\delta(m_1 + l_1 - m_2 + l_2 + hF_P)\delta(m_1 - l_1 - m_2 - l_2 - hF_P)
\end{aligned}
$$
$$(53)$$

Substituting (53) into (52), yields

$$
\begin{aligned}
&E[TDCI(q_r, p_v, r_a)^2]\\
&= \frac{B^2 M^4 A^4 N^2}{4F_s^2} + \frac{BM^3 N A^2 \sigma^2}{2F_s} + \frac{BM^2 \sigma^4 N}{2F_s} \qquad (54)
\end{aligned}
$$

Substituting (54) and (51) into (50), yields

$$
\text{var}[TDCI(q_r, p_v, r_a)] = \frac{BM^3 N A^2 \sigma^2 + BM^2 \sigma^4 N}{2F_s} \qquad (55)
$$

Substituting (55) and (49) into (48), one has

$$
SNR_{out} = \frac{NB}{2F_s} \frac{M^2 SNR_f^2}{M SNR_f + 1} \qquad (56)
$$

Substituting (46) into (56), one has

$$
SNR_{out} = \frac{M^2 \frac{F_s \eta^2}{BN} SNR_{in}^2}{2\left(M \frac{F_s \eta}{BN} SNR_{in} + 1\right)} \qquad (57)
$$

APPENDIX B

In order to clearly illustrate the effect of the cross-term, three cases are discussed. Denote the autocorrelation fold factor and autocorrelation base band velocity of v_i by N_i and v_{0i}, respectively.

Case 1: $v_i \neq v_j$ or $a_i \neq a_j$

In this case,

$$
\begin{aligned}
&C_{1-cross,i,j}(f, t_m, f_{\tau m})\\
&= A_{3i}A_{3j}rect\left(\frac{f}{B}\right)\\
&\quad \times \exp\left[-j2\pi\left(\frac{f + f_c}{f_c}\right)\frac{4\Delta R_0 + 4\Delta v t_m + 2\Delta a t_m^2}{\lambda}\right]\\
&\quad \times [P_1(f, t_m, f_{\tau m}) + P_2(f, t_m, f_{\tau m})] \qquad (58)
\end{aligned}
$$

where

$$
\begin{aligned}
&P_1(f, t_m, f_{\tau m})\\
&= \int \exp\left\{j2\pi\frac{f + f_c}{f_c}\left[\begin{array}{l}
\left(f_{\tau m} - \frac{2\Delta a}{\lambda}\right)\left(\tau_m + \frac{h}{2}\right)^2\\
+ \frac{4\nabla v}{\lambda}\left(\tau_m + \frac{h}{2}\right)\\
+ \frac{4\nabla a}{\lambda}t_m\left(\tau_m + \frac{h}{2}\right)
\end{array}\right]\right\}d\tau_m
\end{aligned}
$$
$$(59)$$

$$
\begin{aligned}
&P_2(f, t_m, f_{\tau m})\\
&= \int \exp\left\{j2\pi\frac{f + f_c}{f_c}\left[\begin{array}{l}
\left(f_{\tau m} - \frac{2\Delta a}{\lambda}\right)\left(\tau_m + \frac{h}{2}\right)^2\\
- \frac{4\nabla v}{\lambda}\left(\tau_m + \frac{h}{2}\right)\\
- \frac{4\nabla a}{\lambda}t_m\left(\tau_m + \frac{h}{2}\right)
\end{array}\right]\right\}d\tau_m
\end{aligned}
$$
$$(60)$$

Obviously, $P_1(f, t_m, f_{\tau m})$ and $P_2(f, t_m, f_{\tau m})$ cannot be effectively integrated, making the whole cross-term spread in TDCI domain.

Case 2: $v_i = v_j, a_i = a_j, n \neq N_i$

In this case, $\Delta v = v_i, \Delta a = a_i$, and

$$
\begin{aligned}
&C_{2-n-cross,i,j}(f, f_{tm}, f_{\tau m})\\
&= 2A_{3i}A_{3j}rect\left(\frac{f}{B}\right)\exp\left[-j2\pi(f + f_c)\frac{4\Delta R_0}{c}\right]\\
&\quad \times \delta\left(f_{\tau m} - \frac{2a_i}{\lambda}\right)\\
&\quad \times \delta\left(\frac{f + f_c}{f_c}\left(\frac{4v_{0i}}{\lambda} - f_{tm}\right) + f\frac{4(N_i - n)v_{ab}}{c}\right) \qquad (61)
\end{aligned}
$$

Similar to $C_{2-N_k-others}(f, f_{tm}, f_{\tau m})$, due to the 2nd Dirac delta function, the cross-term cannot be finally accumulated along f- axis by IFT operation.

Case 3: $v_i = v_j, a_i = a_j, n = N_i$

In this case, $\Delta v = v_i, \Delta a = a_i$, and

$$
\begin{aligned}
& TDCI_{n-cross,i,j}\left(t', f_{tm}, f_{\tau m}\right) \\
&= 2A_{3i}A_{3j} \exp\left[-j2\pi \frac{4\Delta R_0}{\lambda}\right] \delta\left(f_{\tau m} - \frac{2a_i}{\lambda}\right) \\
&\quad \times \delta\left(f_{tm} - \frac{4v_{0i}}{\lambda}\right) \operatorname{sin} c\left[B\left(t' - \frac{4\Delta R_0}{c}\right)\right]
\end{aligned} \quad (62)
$$

Clearly, under this circumstance, the cross-term can be accumulated in TDCI domain. Fortunately, both the integrated auto-terms and cross-term reflect the velocity and acceleration accurately, by which the RCM and DFM are completely compensated. Afterwards, according to the procedure of the proposed algorithm, the two targets can be accumulated and detected in range-Doppler frequency domain simultaneously where no cross-term exists.

In conclusion, combing the three cases, the cross-term cannot affect the performance of the proposed algorithm and can be ignored.

REFERENCES

[1] J. Zheng, T. Su, W. Zhu, X. He, and Q. H. Liu, "Radar high-speed target detection based on the scaled inverse Fourier transform," *IEEE J. Sel. Top. Appl. Earth Observ. Remote Sens.*, vol. 8, no. 3, pp. 1108–1119, Mar. 2014.

[2] Z. Sun, X. Li, W. Yi, G. Cui, and L. Kong, "Detection of weak maneuvering target based on keystone transform and matched filtering process," *Signal Process.*, vol. 140, pp. 127–138, Nov. 2017.

[3] J. Zheng, T. Su, H. Liu, G. Liao, Z. Liu, and Q. H. Liu, "Radar high-speed target detection based on the frequency-domain deramp-keystone transform," *IEEE J. Sel. Topics Appl. Earth Observ. Remote Sens.*, vol. 9, no. 1, pp. 285–294, Jan. 2016.

[4] J. Zhang, T. Su, J. Zheng, and X. He, "Novel fast coherent detection algorithm for radar maneuvering target with jerk motion," *IEEE J. Sel. Topics Appl. Earth Observ. Remote Sens.*, vol. 10, no. 5, pp. 1792–1803, May 2017.

[5] X. Li, G. Cui, W. Yi, and L. Kong, "A fast maneuvering target motion parameters estimation algorithm based on ACCF," *IEEE Signal Process. Lett.*, vol. 22, no. 3, pp. 265–269, Mar. 2015.

[6] X. Rao, W. Li, J. Xie, J. Su, and H. Tao, "Long-time coherent integration detection of weak manoeuvring target via integration algorithm, improved axis rotation discrete chirp-Fourier transform," *IET Radar, Sonar Navigat.*, vol. 9, no. 7, pp. 917–926, Aug. 2015.

[7] P. Huang, G. Liao, Z. Yang, X.-G. Xia, J.-T. Ma, and J. Ma, "Long-time coherent integration for weak maneuvering target detection and high-order motion parameter estimation based on keystone transform," *IEEE Trans. Signal Process.*, vol. 64, no. 15, pp. 4013–4026, Aug. 2016.

[8] B. D. Carlson, E. D. Evans, and S. L. Wilson, "Search radar detection and track with the Hough transform. I. system concept," *IEEE Trans. Aerosp. Electron. Syst.*, vol. 30, no. 1, pp. 102–108, Jan. 1994.

[9] B. D. Carlson, E. D. Evans, and S. L. Wilson, "Search radar detection and track with the Hough transform. II. Detection statistics," *IEEE Trans. Aerosp. Electron. Syst.*, vol. 30, no. 1, pp. 109–115, Jan. 1994.

[10] B. D. Carlson, E. D. Evans, and S. L. Wilson, "Search radar detection and track with the Hough transform. III. Detection performance with binary integration," *IEEE Trans. Aerosp. Electron. Syst.*, vol. 30, no. 1, pp. 116–125, Jan. 1994.

[11] J. Carretero-Moya, J. Gismero-Menoyo, A. Asensio-Lopez, and A. Blanco-del-Campo, "Application of the radon transform to detect small-targets in sea clutter," *IET Radar, Sonar Navigat.*, vol. 3, no. 2, pp. 155–166, Apr. 2009.

[12] S. Buzzi, M. Lops, and L. Venturino, "Track-before-detect procedures for early detection of moving target from airborne radars," *IEEE Trans. Aerosp. Electron. Syst.*, vol. 41, no. 3, pp. 937–954, Jul. 2005.

[13] P. Huang, G. Liao, Z. Yang, X.-G. Xia, J.-T. Ma, and X. Zhang, "A fast SAR imaging method for ground moving target using a second-order WVD transform," *IEEE Trans. Geosci. Remote Sens.*, vol. 54, no. 4, pp. 1940–1956, Apr. 2016.

[14] W. Yu, W. Su, and H. Gu, "Fast method for radar maneuvering target detection and motion parameter estimation," *Multidimensional Syst. Signal Process.*, vol. 29, no. 4, pp. 1411–1425, Jul. 2017.

[15] D. Zhu, Y. Li, and Z. Zhu, "A keystone transform without interpolation for SAR ground moving-target imaging," *IEEE Geosci. Remote Sens. Lett.*, vol. 4, no. 1, pp. 18–22, Jan. 2007.

[16] S.-S. Zhang, T. Zeng, T. Long, and H.-P. Yuan, "Dim target detection based on keystone transform," in *Proc. IEEE Int. Radar Conf.*, May 2005, pp. 889–894.

[17] X. Rao, H. Tao, J. Su, X. Guo, and J. Zhang, "Axis rotation MTD algorithm for weak target detection," *Digit. Signal Process.*, vol. 26, pp. 81–86, Mar. 2014.

[18] X. Rao, T. Zhong, H. Tao, J. Xie, and J. Su, "Improved axis rotation MTD algorithm and its analysis," *Multidimensional Syst. Signal Process.*, vol. 30, no. 2, pp. 885–902, Apr. 2019.

[19] J. Xu, J. Yu, Y.-N. Peng, and X.-G. Xia, "Radon-Fourier transform for radar target detection, I: Generalized Doppler filter bank," *IEEE Trans. Aerosp. Electron. Syst.*, vol. 47, no. 2, pp. 1186–1202, Apr. 2011.

[20] J. Xu, J. Yu, Y.-N. Peng, and X.-G. Xia, "Radon-Fourier transform for radar target detection (II): Blind speed sidelobe suppression," *IEEE Trans. Aerosp. Electron. Syst.*, vol. 47, no. 4, pp. 2473–2489, Oct. 2011.

[21] J. Yu, J. Xu, Y.-N. Peng, and X.-G. Xia, "Radon-Fourier transform for radar target detection (III): Optimality and fast implementations," *IEEE Trans. Aerosp. Electron. Syst.*, vol. 48, no. 2, pp. 991–1004, Apr. 2012.

[22] X. L. Xiaolong Li, G. C. Guolong Cui, W. Y. Wei Yi, and L. K. L. Kong, "An efficient coherent integration method for maneuvering target detection," in *Proc. IET Int. Radar Conf.*, Hangzhou, China, 2015, pp. 1–6.

[23] X. Rao, H. Tao, J. Su, J. Xie, and X. Zhang, "Detection of constant radial acceleration weak target via IAR-FRFT," *IEEE Trans. Aerosp. Electron. Syst.*, vol. 51, no. 4, pp. 3242–3253, Oct. 2015.

[24] T. Abatzoglou and G. Gheen, "Range, radial velocity, and acceleration MLE using radar LFM pulse train," *IEEE Trans. Aerosp. Electron. Syst.*, vol. 34, no. 4, pp. 1070–1084, Oct. 1998.

[25] X. Chen, J. Guan, N. Liu, and Y. He, "Maneuvering target detection via radon-fractional Fourier transform-based long-time coherent integration," *IEEE Trans. Signal Process.*, vol. 62, no. 4, pp. 939–953, Feb. 2014.

[26] X. Li, G. Cui, W. Yi, and L. Kong, "Coherent integration for maneuvering target detection based on radon-Lv's distribution," *IEEE Signal Process. Lett.*, vol. 22, no. 9, pp. 1467–1471, Sep. 2015.

[27] M.-Q. Li, J. Xu, X. Zhou, L.-C. Qian, T. Long, and M.-M. Bian, "OTHR highly maneuvering target detection via generalized randon-Fourier transform," in *Proc. CIE Int. Conf. Radar (RADAR)*, Guangzhou, China, Oct. 2016, pp. 1–4.

[28] J. Xu, X.-G. Xia, S.-B. Peng, J. Yu, Y.-N. Peng, and L.-C. Qian, "Radar maneuvering target motion estimation based on generalized radon-Fourier transform," *IEEE Trans. Signal Process.*, vol. 60, no. 12, pp. 6190–6201, Dec. 2012.

[29] X. Li, Z. Sun, W. Yi, G. Cui, L. Kong, and X. Yang, "Computationally efficient coherent detection and parameter estimation algorithm for maneuvering target," *Signal Process.*, vol. 155, pp. 130–142, Feb. 2019.

[30] J. Zheng, H. Liu, J. Liu, X. Du, and Q. H. Liu, "Radar high-speed maneuvering target detection based on three-dimensional scaled transform," *IEEE J. Sel. Topics Appl. Earth Observ. Remote Sens.*, vol. 11, no. 8, pp. 2821–2833, Aug. 2018.

[31] K. Jin, G. Li, T. Lai, T. Jin, and Y. Zhao, "A novel long-time coherent integration algorithm for Doppler-ambiguous radar maneuvering target detection," *IEEE Sensors J.*, vol. 20, no. 16, pp. 9394–9407, Aug. 2020.

[32] K. Jin, T. Lai, Y. Wang, G. Li, and Y. Zhao, "Radar coherent detection for Doppler-ambiguous maneuvering target based on product scaled periodic Lv's distribution," *Signal Process.*, vol. 174, Sep. 2020, Art. no. 107617.

[33] J. Zheng, J. Zhang, S. Xu, H. Liu, and Q. H. Liu, "Radar detection and motion parameters estimation of maneuvering target based on the extended keystone transform (July 2018)," *IEEE Access*, vol. 6, pp. 76060–76074, 2018.

[34] J. Zheng, T. Yang, H. Liu, T. Su, and L. Wan, "Accurate detection and localization of UAV swarms-enabled MEC system," *IEEE Trans. Ind. Informat.*, early access, Aug. 11, 2020, doi: 10.1109/TII.2020.3015730.

[35] J. Zheng, H. Liu, and Q. H. Liu, "Parameterized centroid frequency-chirp rate distribution for LFM signal analysis and mechanisms of constant delay introduction," *IEEE Trans. Signal Process.*, vol. 65, no. 24, pp. 6435–6447, Dec. 2017.

[36] X. Li, L. Kong, G. Cui, and W. Yi, "CLEAN-based coherent integration method for high-speed multi-targets detection," *IET Radar, Sonar Navigat.*, vol. 10, no. 9, pp. 1671–1682, Dec. 2016.
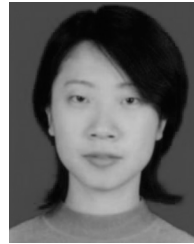
[37] X. Lv, G. Bi, C. Wan, and M. Xing, "Lv's distribution: Principle, implementation, properties, and performance," *IEEE Trans. Signal Process.*, vol. 59, no. 8, pp. 3576–3591, Aug. 2011.

[38] S. Barbarossa, "Analysis of multicomponent LFM signals by a combined Wigner-Hough transform," *IEEE Trans. Signal Process.*, vol. 43, no. 6, pp. 1511–1515, Jun. 1995.

[39] D. Li, M. Zhan, J. Su, H. Liu, X. Zhang, and G. Liao, "Performances analysis of coherently integrated CPF for LFM signal under low SNR and its application to ground moving target imaging," *IEEE Trans. Geosci. Remote Sens.*, vol. 55, no. 11, pp. 6402–6419, Nov. 2017.

[40] P. Wang, H. Li, I. Djurovic, and B. Himed, "Integrated cubic phase function for linear FM signal analysis," *IEEE Trans. Aerosp. Electron. Syst.*, vol. 46, no. 3, pp. 963–977, Jul. 2010.

HAIHONG TAO received the M.S. and Ph.D. degrees from the School of Electronic Engineering, Xidian University, Xi'an, China, in 2000 and 2004, respectively.

She is currently a Professor with the School of Electronic Engineering, Xidian University. Her research interests include radar signal processing and array signal processing.
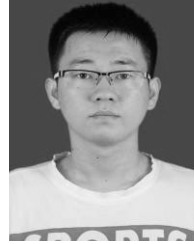
LANGXU ZHAO received the B.S. degree from the School of Electronic Engineering, Xidian University, Xi'an, China, in 2015. He is currently pursuing the Ph.D. degree with the National Laboratory of Radar Signal Processing, Xidian University.

His research interests include maneuvering target enhancement, detection, and parameters estimation.

WEIJIA CHEN received the B.S. degree from Xidian University, Xi'an, China, in 2018, where he is currently pursuing the M.S. degree with the National Laboratory of Radar Signal Processing.

His research interests include passive radar and moving target detection.

• • •